

## Active and stable plasma-enhanced ALD Pt@Ni-YSZ hydrogen electrode for steam reversible solid oxide cells

Hyong June Kim<sup>a,1</sup>, Haoyu Li<sup>b,1</sup>, Daehyun Kim<sup>c,1</sup>, Geonwoo Park<sup>d</sup>, Sung Eun Jo<sup>a</sup>, Kyoungjae Ju<sup>a</sup>, Geongu Han<sup>d</sup>, Yongchai Kwon<sup>e</sup>, Haesun Park<sup>c,\*</sup>, Min Hwan Lee<sup>b,\*\*</sup>, Jihwan An<sup>a,f,\*\*\*</sup>

<sup>a</sup> Department of Mechanical Engineering, Pohang University of Science and Technology (POSTECH), Republic of Korea

<sup>b</sup> Department of Mechanical Engineering, University of California Merced, CA, United States

<sup>c</sup> School of Integrative Engineering, Chung-Ang University, Republic of Korea

<sup>d</sup> Department of Manufacturing System and Design Engineering, Seoul National University of Science and Technology, Republic of Korea

<sup>e</sup> Department of Chemical and Biomolecular Engineering, Seoul National University of Science and Technology, Republic of Korea

<sup>f</sup> Institute for Convergence Research and Education in Advanced Technology, Yonsei University, 50 Yonsei-ro, Seodaemun-gu, Seoul 120-749, Republic of Korea

### ARTICLE INFO

#### Keywords:

Reversible solid oxide cell  
Hydrogen evolution reaction  
Hydrogen oxidation reaction  
Plasma enhanced atomic layer deposition  
Platinum catalyst

### ABSTRACT

Designing and fabricating active and thermally stable bifunctional catalysts with minimal noble metal loadings are crucial for reversible solid oxide cells (rSOCs). This study employed Pt nanoparticles fabricated via plasma-enhanced atomic layer deposition (PEALD) to a nickel-yttria stabilized zirconia (Ni-YSZ) electrode to serve as effective catalysts in fuel cell and electrolysis modes. Despite the minimal Pt catalyst loading ( $<1 \mu\text{g cm}^{-2}$ ), the PEALD Pt@Ni-YSZ catalytic electrode exhibited superior electrochemical performance, (20 % higher than the bare cell), both in the fuel cell and electrolysis modes. Remarkably, this performance is sustained without any degradation over a 50 h duration at 700 °C. Dissimilar stabilization behaviors of the Pt catalysts occurred as distributed fine particles on Ni and anchored coarsened particles at the grain boundaries on YSZ surfaces. Furthermore, the mechanism of the enhanced hydrogen evolution/oxidation reactions with the PEALD Pt@Ni-YSZ electrode was verified using density functional theory simulations.

### 1. Introduction

The production and utilization of hydrogen energy have become essential components in the global energy transition to meet the energy demands of future generations. Reversible electrochemical cells that generate electricity from hydrogen energy in the fuel cell (FC) mode and efficiently decompose steam into storable hydrogen fuel in the electrolysis cell (EC) mode may offer an effective solution for the conversion and storage of renewable energy with hydrogen as an energy carrier. Consequently, they hold great potential for applications in the future energy sector [1–7]. Reversible solid oxide cells (rSOCs) have attracted attention owing to high energy conversion efficiencies because the elevated operating temperature (usually  $> 700\text{--}800$  °C) allows for facile

electrochemical reactions and efficient waste heat utilization compared to other hydrogen energy conversion devices [7–10]. Nonetheless, the commercialization of rSOCs remains limited due to technical challenges such as yet insufficient electrochemical performance (particularly in intermediate temperature range of 500–700 °C), short lifespan, and high system costs associated with the high operating temperatures [6–8]. Consequently, the simultaneous enhancement of the performance and stability of electrodes is an essential issue that must be addressed for the successful commercialization of this technology.

Significant progress has been recently made in SOC electrodes to create catalytically active and thermally stable catalyst-electrode structures: infiltration [11,12], ex-solution [13–15], and novel perovskite development [16–19], mostly for perovskite oxygen electrodes. In

\* Correspondence to: School of Integrative Engineering, Chung-Ang University, 84 Heukseok-ro, Dongjak-gu, Seoul, Republic of Korea.

\*\* Correspondence to: Department of Mechanical Engineering, University of California Merced, 5200 N. Lake Rd, Merced, CA 95343, United States.

\*\*\* Correspondence to: Department of Mechanical Engineering, Pohang University of Science and Technology (POSTECH), 77 Cheongam-ro, Nam-gu, Pohang, Gyeongbuk 37673, Republic of Korea.

E-mail addresses: [parkh@cau.ac.kr](mailto:parkh@cau.ac.kr) (H. Park), [mlee49@ucmerced.edu](mailto:mlee49@ucmerced.edu) (M.H. Lee), [jihwanan@postech.ac.kr](mailto:jihwanan@postech.ac.kr) (J. An).

<sup>1</sup> These authors contributed equally to this work.

particular, the ex-solution of the most catalytically active noble metals has been demonstrated, but only at relatively high concentrations, which are not economically viable for large-scale catalytic uses. Moreover, the substitution of minor amounts of noble metals poses other challenges due to thermodynamic and kinetic factors; that is, the noble metal ions tend to interact more intensely with the perovskite structure, thereby raising the thermodynamic barriers necessary for their ex-solution. At these dilute concentrations, the diffusion processes crucial for bringing ex-solvable ions to the surface significantly influence particle growth, and consequently, the degree of ex-solution [20]. Moreover, the ex-solution of metal catalyst has rarely been reported for fuel electrodes (e.g., Ni-*y*tria stabilized zirconia (YSZ) cermet), due to the restricted capability to dissolve transition metals (e.g., Ni) into lattice in fluorite-structured oxides (e.g., YSZ) of cermet electrodes [21–23].

Atomic layer deposition (ALD), a type of chemical vapor deposition (CVD), offers a versatile approach to produce metal catalysts with high conformality over porous electrodes, with minimal constraints on the selection of metals or supports. Furthermore, ALD enables precise control over the deposition amount at the atomic scale, allowing for minimized precious metal loading. For instance, a Pt loading of < 1/10, compared to the one with infiltrated Pt, on La<sub>0.3</sub>Sr<sub>0.7</sub>TiO<sub>3</sub> (LST) anode by ALD rendered comparable solid oxide fuel cell (SOFC) performance [24]. In another report, ALD Ru-coated samaria-doped ceria (SDC) anode exhibited superior performance with methane fuel to the one with sputtered Pt with only < 1/20 loading [25]. Plasma-enhanced atomic layer deposition (PEALD), which adopts plasma as a reactant, can further accelerate nucleation and grain growth and results in the formation of highly dense catalysts compared to conventional thermal ALD process [26]. Indeed, Fang et al. reported that the oxygen radicals of plasma in PEALD Pt process significantly reduce the nucleation delay in three key ways: (1) supplying active atomic oxygen to the surface, (2) enhancing the oxidation of ligands on the chemisorbed precursor, and (3) promoting Pt nucleation through additional energy provided by the plasma [27]. Such a fast nucleation in PEALD enables the deposition of expensive noble metal catalysts (e.g., platinum group metals) in extremely small amounts over large surface areas. PEALD process is also versatile in synthesizing a wide range of electrocatalysts for various electrochemical reactions, including CO<sub>2</sub> and nitrate reduction [28–30]. Nevertheless, the application of ALD or PEALD catalysts to rSOC fuel electrodes, where hydrogen oxidation and evolution reactions alternately occur, is yet to be demonstrated, even though they may offer an optimal catalyst-electrode design that is not achievable with current fabrication methods.

In this study, an extremely small amount of Pt was deposited on the Ni-YSZ fuel electrode using plasma-enhanced ALD, which can fabricate nanoparticles with higher areal density and more intimate interface quality than conventional ALD in virtue of energetic plasma species, and the resulting electrode was employed as bifunctional fuel electrode of rSOC. The electrochemical performance of rSOC samples with different thicknesses (or cycles) of PEALD Pt catalyst was analyzed. The sample with 10 cycles of PEALD Pt whose Pt loading of only 0.2 µg cm<sup>-2</sup> showed a 20 % increase in maximum power density (548 vs. 479 mW cm<sup>-2</sup> at 700 °C), 25 % reduction in polarization resistance in FC mode, and 18 % higher current density (1260 vs. 1070 mA cm<sup>-2</sup> @1.5 V) in EC mode compared to the pristine Ni-YSZ bare sample at 700 °C, of which the mechanism was confirmed by density functional theory (DFT) simulation. Notably, the fuel cell performance of the the PEALD Pt(10 cycles) @Ni-YSZ sample with dry methane fuel improved by up to 81 % compare to the bare Ni-YSZ sample at 700 °C (246 vs. 446 mW cm<sup>-2</sup>). Furthermore, almost no performance degradation was observed during 100 h of operation at 700 °C in a 50 % humidified environment, which was attributable to the two-track stabilization of Pt particles: coarsened particles anchored between YSZ grains and fine particles sparsely distributed on Ni.

## 2. Experimental

### 2.1. SOC preparation

Reversible solid oxide cells were prepared by screen-printing 5 µm-thick gadolinia-doped ceria (GDC) and 5 µm-thick YSZ on top of 700 µm-thick NiO-YSZ (60:40 wt%) (2 × 2 cm<sup>2</sup>; Kceracell, Korea). All samples had the same oxygen electrode (20 µm -thick) fabricated under the same conditions using LSCF-SDC powder (Fuel Cell Materials, USA) by screen-printing and sintering at 850 °C. Subsequently, a LSCF current collecting layer was deposited by screen-printing and another sintering at 850 °C. The fuel electrode was then reduced under a gas mixture of 95 sccm N<sub>2</sub> and 5 sccm H<sub>2</sub> at 500 °C for 20 h. Pt was deposited on the reduced Ni-YSZ support by PEALD with 5, 10, and 20 cycles, resulting in cells named 5Pt, 10Pt, and 20Pt, respectively (Fig. 1a,b). Samples without an PEALD treatment are named as bare.

### 2.2. PEALD Pt fabrication

The PEALD Pt was processed using a customized PEALD chamber with an inductively coupled plasma (ICP) source, as per our previous study (Fig. S1) [24]. Methyl-cyclopentadienyl tri-methyl platinum (MeCpPtMe<sub>3</sub>) was used as the Pt precursor and oxygen plasma (150 W power) was used as the reactant. The deposition temperature was set at 250 °C, and the Pt precursor was evaporated at 65 °C. Argon gas was used as the carrier and purging gas. One cycle of PEALD Pt included 1 s Pt precursor pulse, 10 s Pt precursor exposure, 30 s Ar gas purge, 10 s oxygen gas supply, 10 s oxygen plasma exposure, and 30 s Ar gas purge. As a result, metallic Pt was deposited at a growth rate per cycle of 0.55 Å cycle<sup>-1</sup> that also corresponds well to a previous study (Fig. S2) [31].

### 2.3. Physical/chemical characterizations

Micromorphological analysis was conducted using field-emission scanning electron microscopy at an acceleration voltage of 3 kV (SEM, ZEISS, Gemini SEM 500), field-emission SEM with energy dispersive spectrometry (FE-SEM with EDS, JSM 7401 F(JEOL)), and field-emission transmission electron microscopy (FE-TEM, JEM-2200F (JEOL)). X-ray photoelectron spectroscopy (XPS, Nexsa spectrometer) was used to perform chemical composition analysis with a step size of 1 eV step<sup>-1</sup> in the range of 0–1350 eV using an Al K $\alpha$  source gun. Before the XPS analysis, all samples were pre-etched with Ar at 500 eV to eliminate surface contamination. An inductively coupled plasma-optical emission spectrometer (ICP-OES, Thermo Scientific iCAP 7000) was used for bulk Pt loading analysis. Crystal structure analysis was conducted using an X-ray diffractometer (XRD, Bruker, DE/D8 advance) with a step size of 0.02° step<sup>-1</sup> within 20–80° (20) using Cu X-rays (45 kV and 200 mA).

### 2.4. Electrochemical characterizations of SOCs

The fabricated SOCs were tested at 700 °C using a customized probe station. 100 sccm of 50 % humidified hydrogen was supplied to the fuel electrode, while 79 sccm of N<sub>2</sub> and 21 sccm of O<sub>2</sub> were supplied to the oxygen electrode. A potentiostat (BioLogic, SP-200) was used to perform linear sweep voltammetry (LSV), electrochemical impedance spectroscopy (EIS), and galvanostatic stability test. In rSOC mode operation, LSV analysis was performed from 0.3 V to 1.5 V at a scan rate of 20 mV s<sup>-1</sup>. EIS analysis was carried out at 0.7 V, open circuit voltage (OCV), and 1.2 V, controlling the frequency of a sinusoidal AC voltage of 50 mV in amplitude in the frequency range of 3 MHz to 300 mHz. For the rSOC stability test, the device was operated alternately at 500 mA cm<sup>-2</sup> in FC mode and −500 mA cm<sup>-2</sup> in EC mode for 2 h each, for a total of 50 h [32].

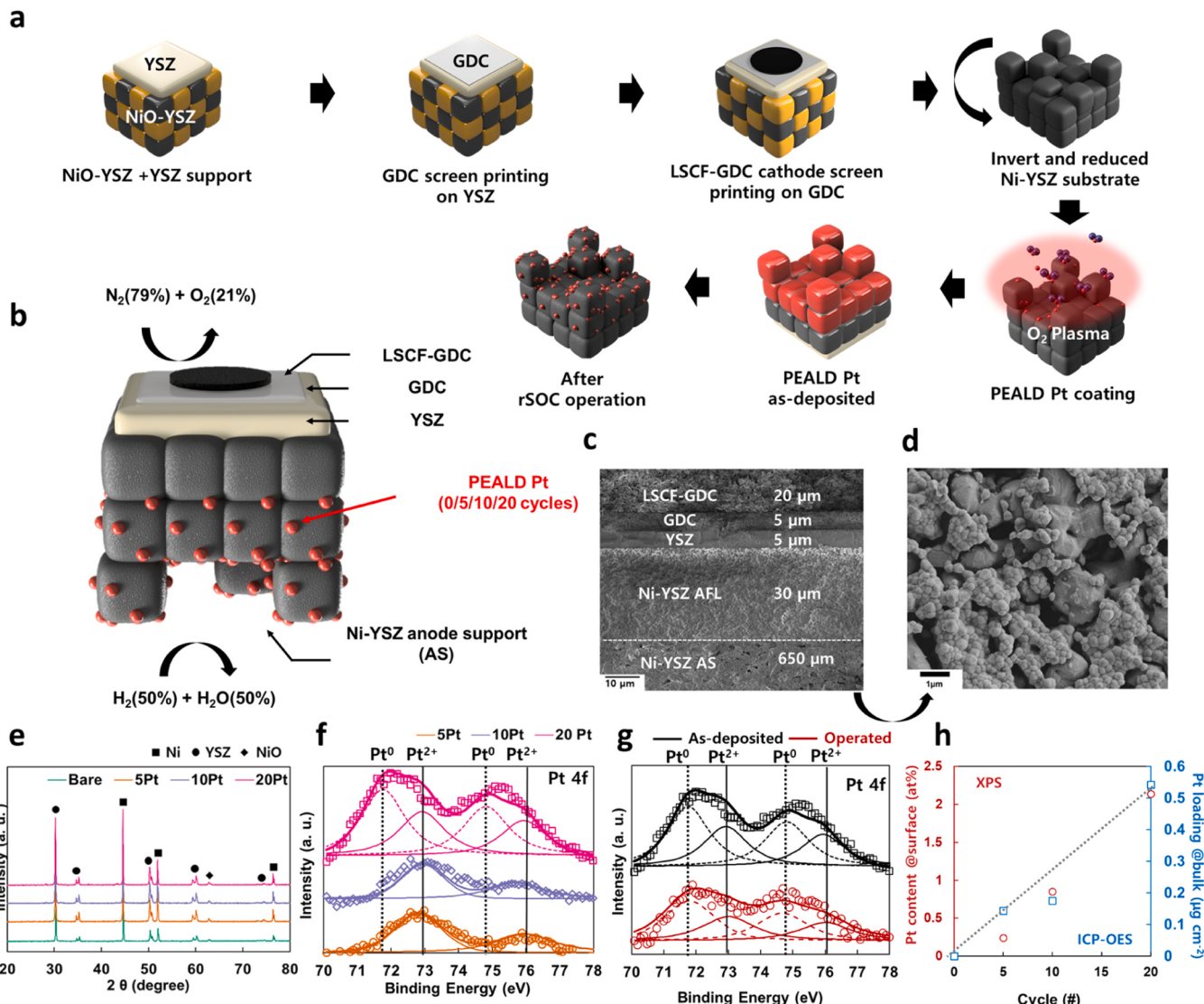


**Fig. 1.** (a) A conceptual illustration of the fabrication process of PEALD@Ni-YSZ anode support. (b) A schematic image of the fabricated rSOC sample. (c) A cross-sectional SEM image of the rSOC sample. (d) A top-view HR-SEM image of porous Ni-YSZ surface after reduction. (e) XRD survey spectra for each sample. (f) XPS spectra (near Pt 4 f) of the PEALD@Ni-YSZ electrodes. (g) XPS spectra (near Pt 4 f) of the as-deposited and after-operated (50 h) samples (20 Pt). (h) Pt contents in PEALD@Ni-YSZ according to the number of ALD cycles measured by XPS (surface) and ICP-OES (bulk).

## 2.5. Density functional theory method

Density functional theory (DFT) [33] calculations were performed as implemented in the Vienna Ab initio Simulation Package (VASP) to investigate the HER and HOR reactions on the PEALD Pt catalyst. The generalized gradient approximation (GGA) method of Perdew-Burke-Ernzerhof functional [34] has been used to describe the electron exchange-correlation functional. The core and the valence electrons have been described by the PAW potentials [35] and the plane-wave basis set [36] with a cutoff energy of 400 eV. The Gamma-centered k-point sampling method was used with the mesh of  $1 \times 2 \times 1$ . All structures have been relaxed to the atomic force tolerances of  $0.03 \text{ eV } \text{\AA}^{-1}$ .

To model the Pt-YSZ cermet, the two units of (1 1 1) YSZ slab with three layers of Zr/Y were connected to create one slab, which had 12 Å in the x-direction, 7 Å in the y-direction and a vacuum region of 20 Å in the z-direction. The four Y atoms replaced four Zr atoms (two from top layer and two from second layer). The oxygen enriched YSZ (YSZ+O) was constructed by adding oxygen atom to vacancies in the second oxygen layer. Initial Pt cluster is composed of three layers of 18 Pt atoms

with nine, six, and three atoms per bottom, medium, and upper layer, respectively. The Pt cluster was incorporated on top of YSZ and YSZ+O surfaces to the gas phase. The most stable (1 1 1) facet of Pt is exposed, resulting in the (1 1 1) surface of Pt being attached to the one unit of YSZ and YSZ+O surfaces with sustained periodicity in the y direction. The bottom multilayer of all slab models was fixed. Further details about the DFT calculations are also provided in the [supplementary material](#).

## 3. Results and discussion

### 3.1. Compositional and structural characterization

The cross-sectional SEM image of the fabricated rSOC sample (**Fig. 1c**) shows Ni-YSZ anode support (AS), anode functional layer (AFL), GDC/YSZ bilayer electrolyte, and LSCF-GDC cathode. **Fig. 1d** reveals the pore generation of the Ni-YSZ surface after reduction process, through which the Pt precursors can infiltrate. The infiltration depth of the PEALD Pt was estimated to be approximately 50 μm (**Fig. S3**). An XRD analysis of the reduced Ni-YSZ (**Fig. 1e**) exhibits mostly metallic Ni (JCPDS card no.: 00-004-0850) and YSZ (JCPDS card

no.: 00-030-1468) peaks with marginal contribution from NiO (JCPDS card no.: 04-0835) phase. Fig. 1f depicts high resolution XPS spectra near Pt 4 f peak of the as-deposited ALD Pt on Ni-YSZ samples. The peak observed at  $\sim$ 71.7 eV is attributed to metallic Pt, while the peak at  $\sim$ 73.0 eV is associated with oxidized Pt (PtO) [37]. It is notable that the relative intensity of PtO peak increases as the thickness of Pt decreases, indicating the existence of a PtO phase on the surface of ALD Pt particles. This is due to the combustion-like nature of the ligand exchange reaction in the ALD Pt process used in this study, which forms a topmost PtO layer. This layer can be easily reduced to metallic Pt during the pre-reduction process of cell operation [38]. Fig. 1g presents the XPS spectra of the as-deposited and after-operation (20Pt) samples. Negligible changes in oxidation states were observed due to XPS peak shifts. However, a decrease in peak intensity was noted, likely due to the agglomeration of Pt particles during operation. While Pt phase is not observed in the XRD spectra due to extremely small amount, Pt content is clearly shown in the XPS (at surface) and ICP-OES (in bulk) spectra (Fig. 1h). The Pt atomic ratios on Ni-YSZ surface from XPS analysis for the 5Pt, 10Pt, and 20Pt samples are 0.2, 0.6, and 2.1 at%, respectively, while the Pt loading in Ni-YSZ bulk determined by ICP-OES analysis are 0.14, 0.18, and 0.54  $\mu\text{g cm}^{-2}$ , respectively.

Fig. 2 demonstrates the morphological changes of PEALD Pt@Ni-YSZ anode surface after rSOC operation for 50 h at 700 °C and 50 % humidity conditions. Overall, the Ni surface exhibits relatively large grain morphologies covered with Pt particles shown as fine and bright structures in inlens mode micrographs, while the granular YSZ surface is decorated with larger agglomerated Pt particles depicted as red dots in SE2 mode micrographs (also see Fig. S4 for compositional analysis). The inlens detector, positioned in the column above the specimen, efficiently captures secondary electrons directly from the sample, resulting in images that provide enhanced surface detail; therefore the fine Pt structure on Ni surface is more clearly shown in inlens mode images [39]. As the cycle number increases, the fine Pt particles are shown to be more

densely and uniformly distributed over Ni surface, resulting in the majority of Ni surface is finally covered with Pt in the 20Pt sample (Fig. 2h). In contrast, the Pt particles on YSZ are shown even larger as a result of agglomeration, preferentially anchored to the grain boundaries (Fig. 2c, d,j) or at the junction between Ni and YSZ (Fig. S5). Fig. 2i shows the schematic depicting the morphological evolution of PEALD Pt on the Ni-YSZ surface, which may be associated with multiple mechanisms including [40–50]: 1) the tendency for metal migration towards locations of higher surface energy such as grain boundaries or concave sites, and/or 2) the reduction of oxidized Pt particle into metallic Pt that can lead to faster agglomeration due to oxygen depletion near grain boundaries or Ni-YSZ junctions during electrolysis.

In-depth TEM analysis was conducted to observe the morphological evolution of Pt particles at various stages of the rSOC operation under alternating EC and FC modes (Fig. 3 and S6). Fig. 3b-d demonstrate the morphological evolution of ALD Pt particles at different stages of repeated rSOC operation in Fig. 3a. In an as-deposited sample, fine Pt particles are densely distributed on YSZ surface (arrows in Fig. 3b). After 2 h of EC mode operation, the partial coarsening of Pt particles is evident, leading to the formation of a larger particle (approximately 10 nm; arrowed in Fig. 3c). After 8 h of cyclic operations between EC and FC modes, fine particles disappear and coarsened particles of approximately 8 nm in diameter became predominant (Fig. 3d). Interestingly, the average diameter of the Pt particles was maintained at 8–10 nm in diameter for up to 50 h (Fig. 3e,f).

### 3.2. Electrochemical characterization

Fig. 4 presents the electrochemical analysis of the cells operated in fuel cell mode with 50 % humidified hydrogen at 700 °C. Fig. 4a,b display the I-V-P results at 700 °C and maximum power density (MPD) comparison at temperature ranges of 580–700 °C, respectively. The 10Pt sample exhibited the highest performance at all temperatures including

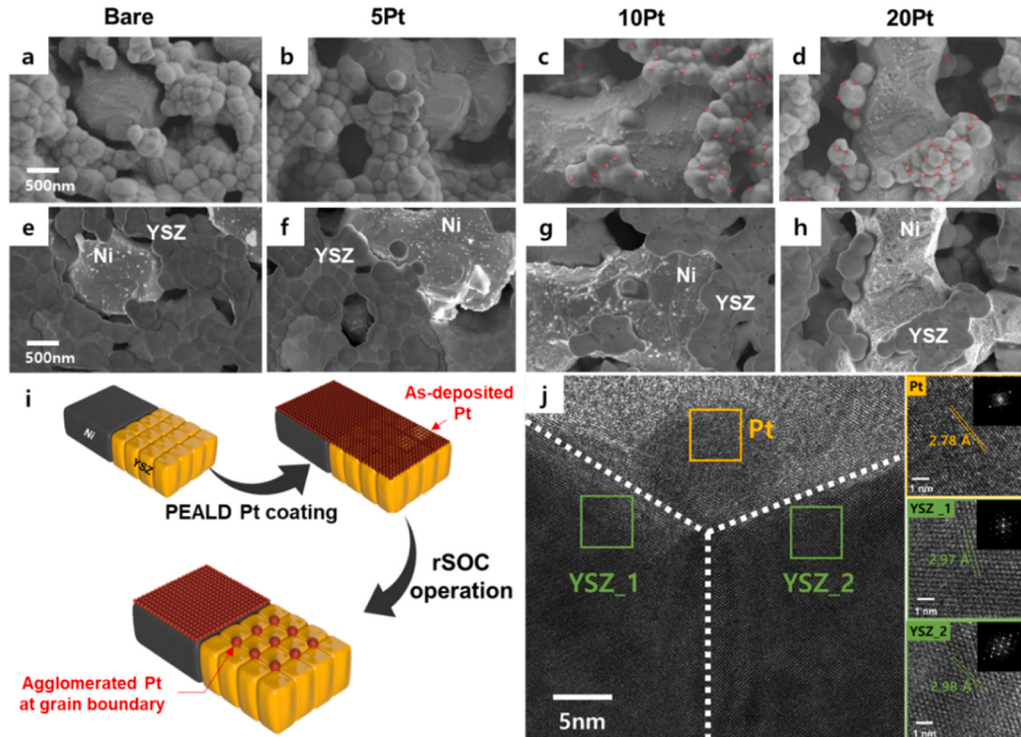


**Fig. 2.** (a-h) Top-view SEM images of PEALD Pt@Ni-YSZ electrodes after rSOC operation in SE2 mode (a-d) and inlens mode (e-h): (a,e) bare, (b,f) 5Pt, (c,g) 10Pt, and (d,h) 20Pt samples. (i) A schematic diagram depicting Pt particle agglomeration and stabilization on Ni-YSZ substrate. Scale bars are identical for all SEM images. (j) Cross-sectional TEM image of a Pt particle on the YSZ grain boundary; the lattice spacing values of Pt (2.78  $\text{\AA}$ ) and YSZ (2.97–2.98  $\text{\AA}$ ) correspond to Pt(110) and 8YSZ(111), respectively.

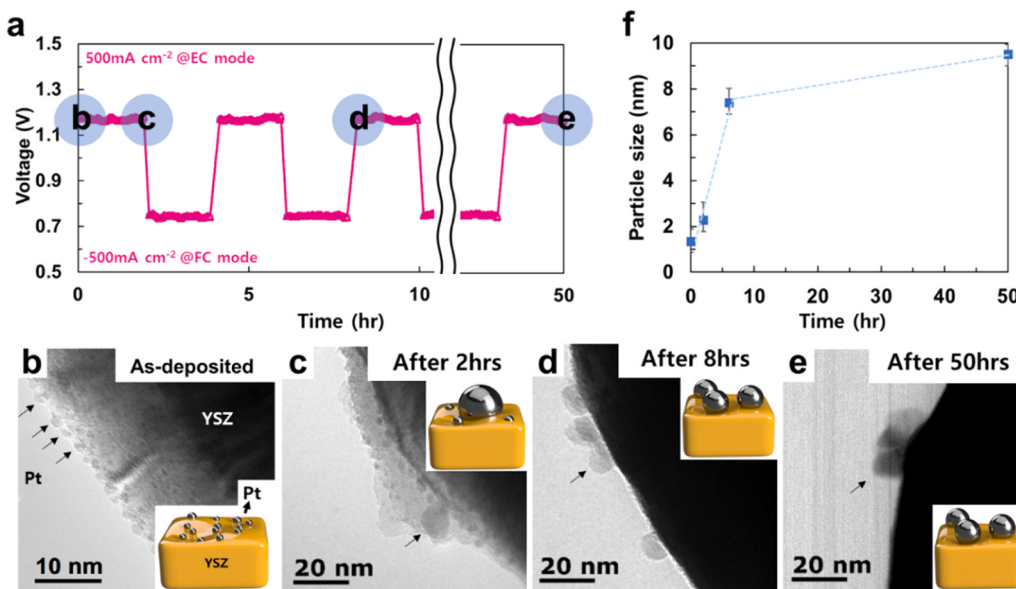


**Fig. 3.** TEM analysis of morphological changes of PEALD Pt particles on YSZ surface with rSOC cycle condition: (a) Voltage profiles in rSOC operation and the points where TEM images are recorded in (b-d); (b) as-deposited, (c) after 2 h, (d) after 8 h and (e) after 50 h (black arrows indicate Pt particles). (f) Summary of Pt particle size change with operation time.

548 mW cm<sup>-2</sup> at 700 °C, which is 20 % greater than the performance of the bare sample without PEALD Pt (479 mW cm<sup>-2</sup>). In the test with pure dry hydrogen, the 10Pt sample exhibited the highest performance of 818 mW cm<sup>-2</sup> at 700 °C, which is also 20 % greater than the performance of the bare sample without PEALD Pt (679 mW cm<sup>-2</sup>) (Fig. S7). Fig. 4c presents the EIS spectra that are divided into the ohmic impedance part (>100 kHz) that does not change with cell voltage and the polarization impedance part (< 100 kHz) that changes with cell voltage. The polarization impedance can be further deconvoluted to the fuel electrode contribution at high frequency (~100–1 kHz) and the oxygen electrode contribution at low frequency (~1 kHz–1 Hz) (Fig. S8). The variation in the arc sizes with cell voltage allows for the differentiation between ohmic resistance and polarization resistance (Fig. S8). All samples exhibited similarly low ohmic resistances of approximately 0.2 Ω cm<sup>2</sup>. Fig. 4d shows the Arrhenius plot of fuel electrode polarization obtained at the cell voltage of 0.7 V. The calculated activation energies for the bare, 5Pt, 10Pt, and 20Pt samples are 1.39, 1.34, 1.25, and 1.41 eV, respectively. This confirms that PEALD Pt is beneficial in lowering the activation barrier for HOR occurring on fuel electrodes. Additionally, Fig. 4e shows the I-V-P curves comparing the electrochemical performances of the bare sample and the 10Pt sample under dry methane operation at 700 °C, to further compare the catalytic activity of PEALD Pt-coated anode for methane oxidation reaction. The 10Pt sample and bare sample exhibited power densities of 446 mW cm<sup>-2</sup> and 246 mW cm<sup>-2</sup>, respectively. Fig. 4f presents the comparison of MPD for the bare and the 10Pt samples in the temperature range of 580–700 °C under dry methane. The bare sample demonstrated MPDs of 93, 149, 185, and 246 mW cm<sup>-2</sup> at 580, 620, 660, and 700 °C, respectively, while the 10Pt sample exhibited MPDs of 96, 196, 294, and 446 mW cm<sup>-2</sup> at the same temperatures, highlighting the significant improvement in performance with PEALD Pt coating. Fig. S9 shows the IVP curves and post-operation SEM images of the electrode surfaces for both the bare and the 10Pt samples; the bare sample surface revealed the formation of carbon fibers, indicating severe carbon coking, while the surface of the PEALD Pt-coated sample showed no visible carbon fiber formation, which suggests that the PEALD Pt particles may mitigate carbon deposition, as has been reported in previous studies [51].

Fig. 5a presents polarization curves of the studied cells spanning both FC and EC modes at 700 °C with 50 % humidity. The current densities at thermo-neutral voltage (TNV, 1.29 V) of the bare, 5Pt, 10Pt, and 20Pt

samples was 646, 757, 809, and 653 mA cm<sup>-2</sup>, respectively, showing an 18 % performance improvement in the 10Pt sample compared to the bare sample. Additionally, at a cell potential of 1.5 V, the samples exhibited current densities of 1070, 1110, 1260, and 1060 mA cm<sup>-2</sup>, respectively. Fig. 5b compares the performance of each sample under rSOC operating conditions (700 °C, 50 % humidity) both in FC and EC modes. Notably, both FC and EC modes demonstrate a consistent trend across the samples, with the 10Pt sample exhibiting the highest performance, followed by 5Pt, bare, and 20Pt. This trend is further corroborated by the polarization resistances derived from EIS measurements at OCV of 0.98 V and 700 °C (Fig. 5c), which were 0.25, 0.24, 0.21, and 0.26 Ω·cm<sup>2</sup> for the bare, 5Pt, 10Pt, and 20Pt samples, respectively. Additionally, this trend extends to the activation energy for HER. The activation energies of polarization resistance at the fuel electrode, obtained at 1.2 V, are 1.36, 1.27, 1.18, and 1.46 eV, for the bare, 5Pt, 10Pt, and 20Pt samples, respectively. These confirm that the kinetics of HER are similarly enhanced by PEALD Pt decoration, akin to the HOR. More detailed EIS analysis results, including comparisons of the results at the same current density vs. potential and comparisons between samples at varying voltages, are available in Figs. S10 and S11.

In a 50h-long OCV test (Fig. 6a), all samples maintained the OCV of approximately 0.97 V during the test duration, exhibiting a difference of < 3 % from the theoretical value. Notably, none of the samples exhibited a meaningful degradation in OCV value over time, despite minor variations. Furthermore, in a durability test involving cyclic rSOC operations between FC and EC modes, each at 500 mA cm<sup>-2</sup> for 2 h, all samples with PEALD Pt decoration demonstrated highly stable performance for 50 h, akin to the bare sample, as evidenced in Fig. 6b. The samples with PEALD Pt@Ni-YSZ electrodes consistently showed lower polarization resistance compared to the bare sample throughout the 50 h operation (Fig. 6b,c). In the prolonged operation for 100 h, the 10Pt sample showed lower voltage degradation rate compared to the bare sample, both in FC (0.069 (10Pt) vs. 0.120 % h<sup>-1</sup> (bare) at -500 mA cm<sup>-2</sup>) and EC modes (0.072 (10Pt) vs. 0.078 % h<sup>-1</sup> (bare) at +500 mA cm<sup>-2</sup>) (Fig. 6d). Such a high stability of Pt particles may be partly associated with their behavior at grain boundaries, which significantly mitigates coarsening kinetics. As demonstrated by Ahn et al., Pt particles tend to migrate toward and stabilize at grain boundaries due to the lower chemical potential in these regions. The concave geometry of grain boundaries offers an energetically favorable

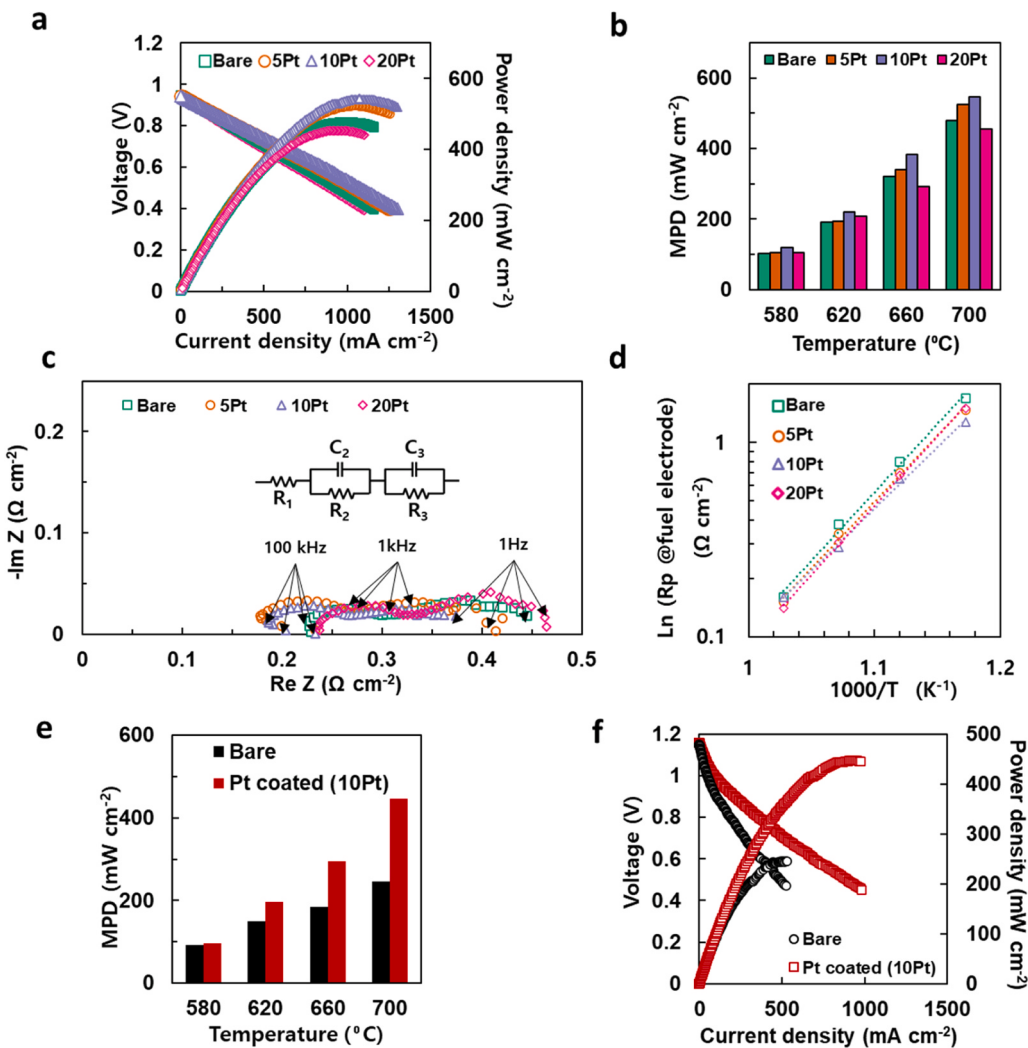


**Fig. 4.** Comparison of electrochemical performances in fuel cell mode for the rSOCs with PEALD Pt@Ni-YSZ electrodes: (a) I-V-P characteristics. (b) Comparison of maximum power density (MPD) at temperature range of 580–700 °C. (c) EIS spectra with equivalent circuit model. (d) Arrhenius plot of polarization resistances ( $R_p$ , corresponding to  $R_2$  in the equivalent circuit model) at the fuel electrode (at 0.7 V). (e) I-V-P curves of bare and Pt-coated (10 Pt) samples operated in fuel cell mode at 700 °C using dry methane fuel. (f) MPD at temperature range of 580–700 °C.

environment, effectively reducing the likelihood of particle coarsening and agglomeration. This stabilization mechanism appears to play a crucial role in maintaining the dispersion and catalytic activity of Pt particles over extended periods [50]. Additionally, it is notable that the improvement in the degradation rate of the sample with PEALD Pt@Ni-YSZ electrode is significant in FC mode, while marginal in EC mode. We speculate that such a difference may stem from the dissimilar stabilization mechanism of Pt particles between FC mode and EC mode operations.

### 3.3. Discussion

The electrochemical analysis results shown above can be summarized in two aspects: 1) the addition of a small amount of PEALD Pt up to 10 cycles improves the electrochemical performance, and 2) the excessive coverage of ALD Pt (20 cycles) adversely affects the electrochemical performance of the rSOC with the Ni-YSZ fuel electrode in both HER (EC mode) and HOR (FC mode).

First, DFT calculations were performed to understand the improved HER and HOR performances on the Pt-YSZ interface compared to the bare YSZ surface (Fig. 7). On the YSZ surface, the HER initiated by adsorption of  $H_2O$  molecule was followed by the dissociation of hydrogen and its adsorption on surface oxygens [52]. This reaction path

and the free energies of the reaction are illustrated in Fig. 7a (red color scheme). The reaction mechanism of the HER on the Pt-YSZ interface was motivated by a similar reaction of the Ni-YSZ cermet [53]. On the Pt-YSZ interface, the  $H_2O$  molecule is absorbed on the boundary between Pt and YSZ followed by dissociation of  $H_2O$ . The dissociated H atoms spill over to the Pt surface and the remaining H also diffuse to the Pt surface, forming  $H_2$  molecule. This process, along with its associated free energy profile, is depicted in Fig. 7a, utilizing a blue color scheme. The energy barrier on the YSZ surface was measured at 1.94 eV, which is significantly lowered to 1.01 eV with the introduction of Pt clusters. This is also lower than the thermodynamic barrier found in the Ni-YSZ cermet, which is 1.47 eV [54]. For all catalysts examined, the thermodynamic energy barrier was observed during the  $H_2O$  adsorption process, with subsequent reaction steps being exergonic. This indicates that the incorporation of Pt enhances the adsorption process of  $H_2O$  molecules, thereby facilitating the overall reaction.

The HOR, wherein absorbed hydrogen atoms react with the surface oxygen to successively create water molecules, necessitates the diffusion of bulk oxygen to the surface, thereby inducing an oxygen-enriched surface (YSZ + O) [55]. To ascertain the thermodynamic propensity for the formation of an oxygen-enriched surface, we have compared the enthalpy of a Pt-YSZ +  $O_2$  gas with that of Pt-YSZ + O as shown in Fig. S12. The YSZ without any metal exhibits a substantial

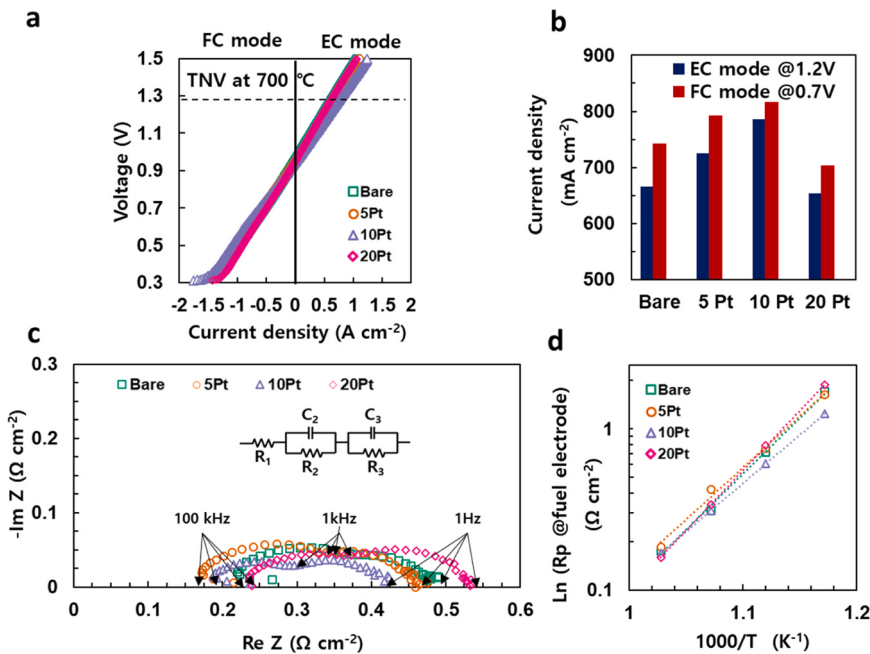


**Fig. 5.** Electrochemical performance comparison in rSOC mode of the cells with PEALD Pt@Ni-YSZ electrodes under 50 % humidified conditions. (a) I-V characteristics at  $700^\circ\text{C}$  in FC/EC modes. (b) Current density comparison in FC (0.7 V) and EC (1.2 V) modes. (c) EIS spectra of the samples at  $700^\circ\text{C}$  at 1.2 V. (d) Arrhenius plot of polarization resistance ( $R_p$ ) at the fuel electrode obtained at 1.2 V.

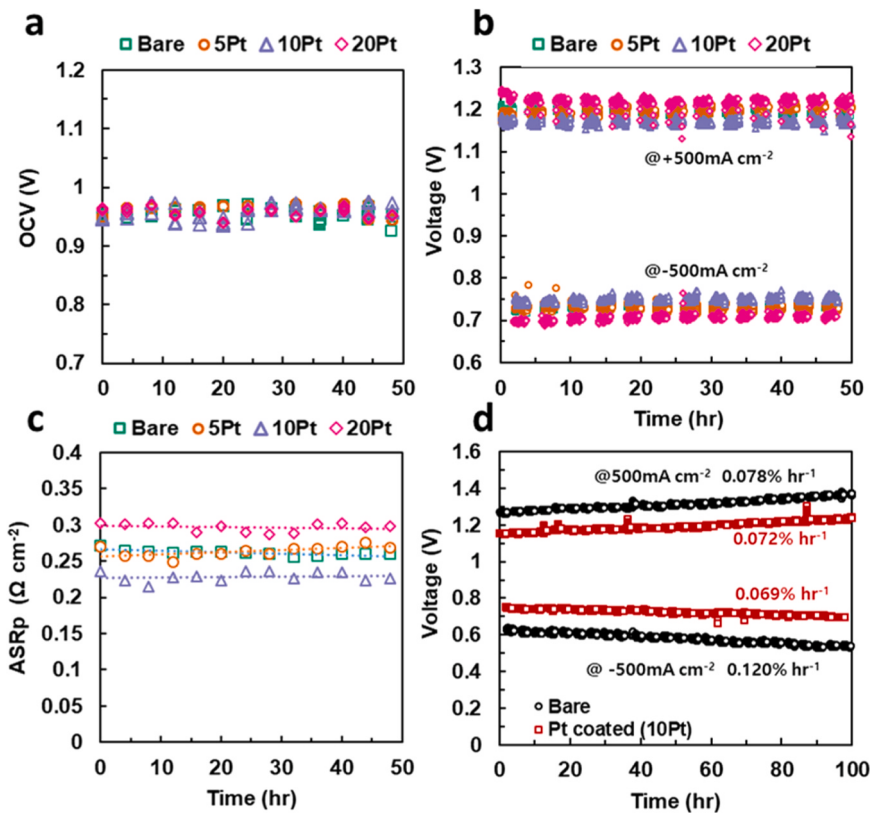


**Fig. 6.** (a) OCV stability evaluation at  $700^\circ\text{C}$  for 50 h. (b) Durability test with cyclic rSOC operation where galvanostatic measurements alternate between FC and EC modes, both at  $500 \text{ mA cm}^{-2}$ . Testing was performed at  $700^\circ\text{C}$  under 50 % humidity condition. (c) Polarization resistance changes determined from EIS measurements at  $500 \text{ mA cm}^{-2}$  during the cyclic durability test. (d) 100 h operation of the bare and 10 Pt samples at  $700^\circ\text{C}$  under 50 % humidity condition.

thermodynamic driving force ( $0.75 \text{ eV atom}^{-1} = 72 \text{ kJ mol}^{-1}$ ) that preserves oxygen vacancies in proximity to the surface. This leads us to the assumption that the thermodynamics do not favor the migration of

oxygen into these vacancy sites, and it appears that the oxygens provided for the HOR are quickly utilized or diffuse back to bulk. Pt-YSZ + O demonstrates thermodynamic stability, exhibiting a marginal

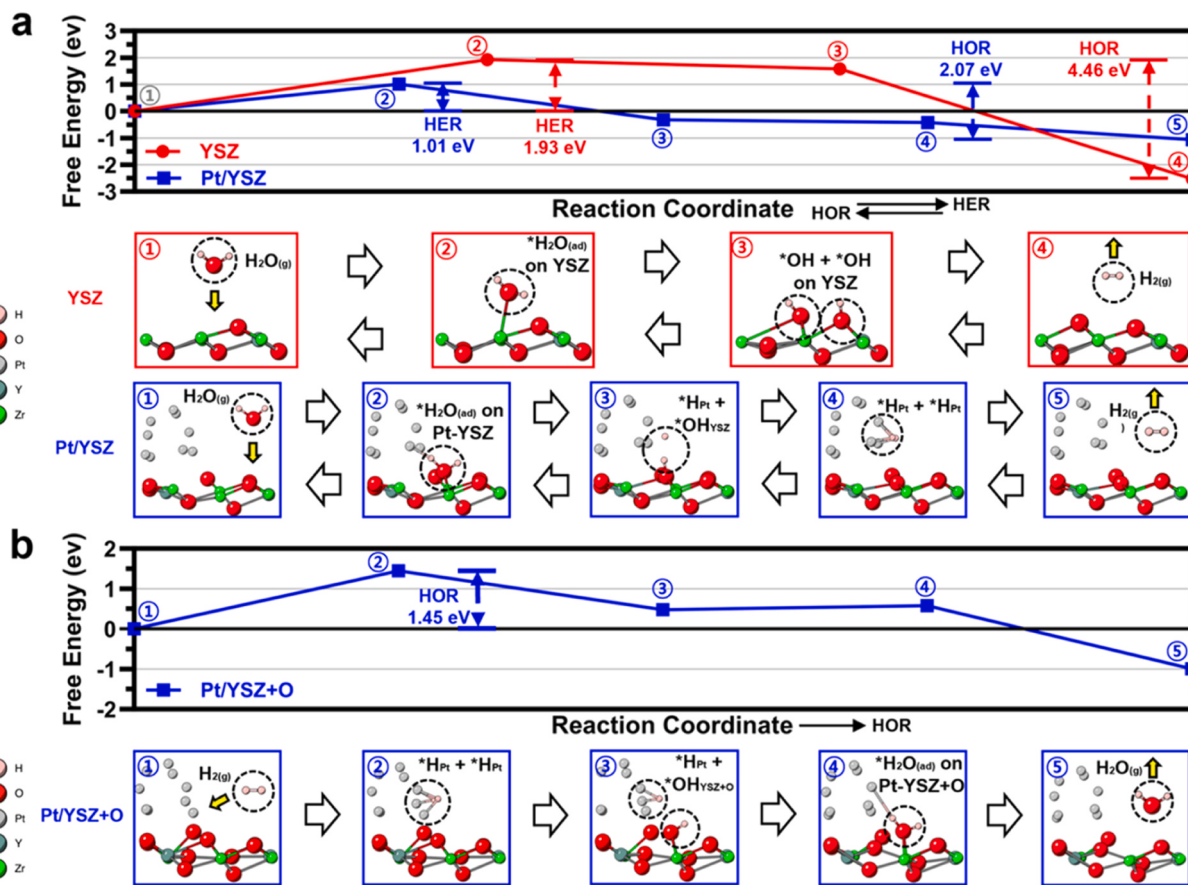


**Fig. 7.** (a) The free energy profile (upper panel) and the illustration of reaction pathways (lower panel) of the HER (left to right) and the HOR (right to left) on YSZ, and Pt-YSZ surface. (b) The free energy profile and the illustration of reaction pathways during the HOR on Pt-YSZ+O surface.

enthalpy difference compared to Pt-YSZ + O<sub>2</sub> (equivalent to 0.02 eV atom<sup>-1</sup> or 2 kJ mol<sup>-1</sup>). This infers a viable thermodynamic transition between Pt-YSZ and Pt-YSZ + O, indicating that the HOR could transpire under either condition.

The free energy profiles and reaction paths of HOR on YSZ and Pt-YSZ cermet are depicted in red and blue color scheme, respectively, in Fig. 7a. The free energy profiles and reaction path of HOR on Pt-YSZ + O is depicted in Fig. 7b. The HOR path constitutes the reverse process of HER, with the reaction proceeding from right to left illustrated in the figure. On YSZ, the dissociated hydrogen atoms bond with surface oxygens and one of the hydrogen atoms diffuse to the other OH, thereby forming a H<sub>2</sub>O molecule. On the Pt-YSZ surface, the hydrogen molecules undergo dissociation on the Pt surface and one of the hydrogen spillover to the oxygen atom at the interface between Pt and YSZ, resulting in the formation of OH. The reaction is completed by the remaining hydrogen on Pt surface migrating to the OH group at the interface, facilitating the formation of a H<sub>2</sub>O molecule. The thermodynamic barrier of HOR on YSZ is identified as 4.46 eV and such large barrier is associated with the H<sub>2</sub> molecule adsorption and dissociation at the surface. In contrast, the barrier on the Pt-YSZ surface is significantly reduced to 2.05 eV. Even compared to the Ni-YSZ cermet, where the thermodynamic barrier is no less than 2.42 eV [54], the Pt-YSZ surface presents even lower energy barrier. This reduction is primarily attributed to the substantial decrease in H<sub>2</sub> dissociation process on Pt surface. Similarly, for the Pt-YSZ + O surface, the process of H<sub>2</sub> adsorption and dissociation becomes thermodynamically more favorable, leading to a reduced migration barrier of 1.45 eV.

Our DFT calculations on Pt-YSZ, along with previous DFT studies on Ni-YSZ, demonstrate that metal cluster formation on the YSZ surface boosts catalytic efficiency for HER and HOR. However, the performance

does not monotonically increase with the amount of Pt added. Instead, peak performance is observed with the 10Pt sample, with a noticeable decline in the 20Pt sample. Given the similarities in Pt cluster formation on YSZ between the 10Pt and 20Pt samples, as shown by our SEM images, the optimal performance in the 10Pt sample and the subsequent drop in the 20Pt sample can be attributed to changes in the Ni metal surface caused by Pt alloying. Ni metal typically exhibits poor activity for water electrolysis, largely due to its strong adsorption ability to hydrogen atoms. Nonetheless, partially alloying the surface with Pt enhances this activity. Norskov, et al. studied the hydrogen adsorption energy ( $\Delta G_H$ ) of host Ni surface with various metal (e.g., Pt) solute coverage using DFT [56]. They showed that the  $\Delta G_H$  maintains 0.1–0.2 eV until the Pt coverage reaches up to 1/3 monolayer (ML), but greatly increases to 0.4–0.5 eV at the Pt coverage of 2/3 ML, which implies that the strong adsorption of hydrogen on Ni surface with excessive Pt coverage. An excessively strong adsorption ability of the catalyst's surface is detrimental to the facile diffusion of hydrogen atoms and the subsequent desorption of molecular byproducts, necessitating an optimal adsorption strength for efficient catalytic turnover. Furthermore, our SEM analyses confirm that the surface of Ni metal in the 20Pt samples exhibits a more coverage by Pt clusters in comparison to the 10Pt samples, resulting in a diminished catalytic efficiency relative to the latter.

#### 4. Conclusion

In this study, we applied PEALD Pt nanoparticles with an ultra-low loading amount of <1  $\mu\text{g cm}^{-2}$  to the Ni-YSZ fuel electrode as active and thermally-stable bifunctional electrochemical catalysts. Dissimilar coarsening behaviors of the Pt particles on the Ni and YSZ surfaces were

elucidated. Electrochemical analysis results showed that the rSOC with optimal PEALD Pt condition (i.e., 10Pt) showed effective improvement by 20 % and 18 % compared to the bare sample in FC mode power density and EC mode current density, respectively. The stability of the rSOC with PEALD Pt@Ni-YSZ was clearly demonstrated without degradation over 100 h at 700 °C. This result is one of the largest electrochemical performance improvements per platinum group metal (PGM) loading when compared to previous reports that employed PGM catalysts fabricated by wet(infiltration), physical vapor deposition (sputtering) or even other ALD methods (Fig. S13). The design and manufacturing of active and stable metal catalyst-cermet electrode composite with minimal metal loading by PEALD shown in this study may have implications for wider applications that require superior performance at elevated temperatures.

### CRediT authorship contribution statement

Hyong June Kim: conceptualization, investigation, data curation, writing – original draft. Haoyu Li: conceptualization, investigation, data curation, writing – original draft. Daehyun Kim: simulation, writing – original draft. Geonwoo Park: methodology. Seung Eun Jo: methodology. Kyongjae Ju: methodology. Geonju Han: methodology. Yongchai Kwon: writing – review & editing. Haesun Park: simulation, supervision, writing – review & editing. Min Hwan Lee: conceptualization, supervision, writing – review & editing. Jihwan An: conceptualization, supervision, writing – review & editing.

### Declaration of Competing Interest

The authors declare that they have no known competing financial interests or personal relationships that could have appeared to influence the work reported in this paper.

### Acknowledgements

This research was supported by Basic Science Research Program through the National Research Foundation of Korea (NRF) funded by the Ministry of Education (NRF-2021R1A6A1A03039981), the National Research Foundation of Korea (NRF) grant funded by the Korea government (MSIT) (No. 2022R1A2C4001205, 2022R1C1C1011660) and, Korea Institute of Energy Technology Evaluation and Planning (KETEP) grant funded by the Korea government (MOTIE) (No. 20213030030040). The authors also acknowledge the support from the U.S. National Science Foundation (DMR 1753383).

### Appendix A. Supporting information

Supplementary data associated with this article can be found in the online version at [doi:10.1016/j.apcatb.2024.124740](https://doi.org/10.1016/j.apcatb.2024.124740).

### Data availability

Data will be made available on request.

### References

- [1] E.D. Wachsman and, K.T. Lee, Lowering the temperature of solid oxide fuel cells, *Science* 334 (2011) 935–939, <https://doi.org/10.1126/science.1204090>.
- [2] R.M. Dell, D.A.J. Rand, Energy storage - a key technology for global energy sustainability, *J. Power Sources* 100 (2001) 2–17, [https://doi.org/10.1016/S0378-7753\(01\)00894-1](https://doi.org/10.1016/S0378-7753(01)00894-1).
- [3] N.L. Panwar, S.C. Kaushik, S. Kothari, Role of renewable energy sources in environmental protection: a review, *Renew. Sustain. Energy Rev.* 15 (2011) 1513–1524, <https://doi.org/10.1016/j.rser.2010.11.037>.
- [4] C. Duan, R. Kee, H. Zhu, N. Sullivan, L. Zhu, L. Bian, D. Jennings, R. O’Hayre, Highly efficient reversible protonic ceramic electrochemical cells for power generation and fuel production, *Nat. Energy* 4 (2019) 230–240, <https://doi.org/10.1038/s41560-019-0333-2>.
- [5] V.T. Giap, S. Kang, K.Y. Ahn, High-efficient reversible solid oxide fuel cell coupled with waste steam for distributed electrical energy storage system, *Renew. Energy* 144 (2019) 129–138, <https://doi.org/10.1016/j.renene.2018.10.112>.
- [6] J. Shin, Y.J. Lee, A. Jan, S.M. Choi, M.Y. Park, S. Choi, J.Y. Hwang, S. Hong, S. G. Park, H.J. Chang, M.K. Cho, J.P. Singh, K.H. Chae, S. Yang, H.-I. Ji, H. Kim, J.-W. Son, J.-H. Lee, B.-K. Kim, H.-W. Lee, J. Hong, Y.J. Lee, K.J. Yoon, Highly active and thermally stable single-atom catalysts for high-temperature electrochemical devices, *Energy Environ. Sci.* 13 (2020) 4903–4920, <https://doi.org/10.1039/D0EE01680B>.
- [7] S.-L. Zhang, H. Wang, M.Y. Lu, A.-P. Zhang, L.V. Mogni, Q. Liu, C.-X. Li, C.-J. Li, S. A. Barnett, Cobalt-Substituted  $\text{SrTi}_{0.3}\text{Fe}_{0.7}\text{O}_3\text{-}\delta$ : a stable high-performance oxygen electrode material for intermediate-temperature solid oxide electrochemical cells, *Energy Environ. Sci.* 11 (2018) 1870–1879, <https://doi.org/10.1039/C8EE00449H>.
- [8] A. Hauch, R. Küngas, P. Blennow, A.B. Hansen, J.B. Hansen, B.V. Mathiesen, M. B. Mogensen, Recent advances in solid oxide cell technology for electrolysis, *Science* 370 (2020) eaba6118, <https://doi.org/10.1126/science.aba6118>.
- [9] R.R. Davda, J.W. Shabaker, G.W. Huber, R.D. Cortright and, J.A. Dumesic, A review of catalytic issues and process conditions for renewable hydrogen and alkanes by aqueous-phase reforming of oxygenated hydrocarbons over supported metal catalysts, *Appl. Catal. B* 56 (2005) 171–186, <https://doi.org/10.1016/j.apcatb.2004.04.027>.
- [10] T. Chen, M. Liu, C. Yuan, Y. Zhou, X. Ye, Z. Zhan, C. Xia, S. Wang, High performance of intermediate temperature solid oxide electrolysis cells using  $\text{Nd}_2\text{NiO}_4\text{-}\delta$  impregnated scandia stabilized zirconia oxygen electrode, *J. Power Sources* 276 (2015) 1–6, <https://doi.org/10.1016/j.jpowsour.2014.11.042>.
- [11] V. Kamboj, S. Raychowdhury and, C. Ranjan, Enabling pure CO<sub>2</sub> reduction on Ni  $\{\text{Cu}\}_x\text{-YSZ}$  electrode via an oxide-mediated mechanism, *Appl. Catal. B* 344 (2015) 123631, <https://doi.org/10.1016/j.apcatb.2023.123631>.
- [12] A. Chrzan, S. Ovtar, P. Jasinski, M. Chen, A. Hauch, High performance  $\text{LaNi}_{1-x}\text{Co}_x\text{O}_3\text{-}\delta$  ( $x = 0.4$  to 0.7) infiltrated oxygen electrodes for reversible solid oxide cells, *J. Power Sources* 353 (2017) 67–76, <https://doi.org/10.1016/j.jpowsour.2017.03.148>.
- [13] Y. Wang, T. Liu, M. Li, C. Xia, B. Zhou, F. Chen, Exsolved Fe-Ni nano-particles from  $\text{Sr}_2\text{Fe}_{1.3}\text{Ni}_{0.2}\text{Mo}_{0.5}\text{O}_6$  perovskite oxide as a cathode for solid oxide steam electrolysis cells, *J. Mater. Chem. A* 4 (2016) 14163–14169, <https://doi.org/10.1039/C6TA06078A>.
- [14] Y.Y. Namgung, J. Hong, A. Kumar, D.-K. Lim and, S.-J. Song, One step infiltration induced multi-cation oxide nanocatalyst for load proof SOFC application, *Appl. Catal. B* 267 (2020) 118374, <https://doi.org/10.1016/j.apcatb.2019.118374>.
- [15] K.J. Kim, C. Lim, K.T. Bae, J.J. Lee, M.Y. Oh, H.J. Kim, H. Kim, G. Kim, T.H. Shin, J. W. Han and, K.T. Lee, Concurrent promotion of phase transition and bimetallic nanocatalyst exsolution in perovskite oxides driven by Pd doping to achieve highly active bifunctional electrodes for reversible solid oxide electrochemical cells, *Appl. Catal. B* 314 (2020) 121517, <https://doi.org/10.1016/j.apcatb.2022.121517>.
- [16] B. Mewafy, F. Paloukis, K.M. Papazisi, S.P. Balomenou, W. Luo, D. Teschner, O. Joubert, A. Le Gal La Salle, D.K. Niakolas, S. Zafeiratos, Influence of surface state on the electrochemical performance of nickel-based cermet electrodes during steam electrolysis, *ACS Appl. Energy Mater.* 2 (2019) 7045–7055, <https://doi.org/10.1021/acsaem.9b00779>.
- [17] B. Mewafy, F. Paloukis, K.M. Papazisi, S.P. Balomenou, W. Luo, D. Teschner, O. Joubert, A. Le Gal La Salle, D.K. Niakolas, S. Zafeiratos, Influence of surface state on the electrochemical performance of nickel-based cermet electrodes during steam electrolysis, *ACS Appl. Energy Mater.* 2 (2019) 7045–7055, <https://doi.org/10.1021/acsaem.9b00779>.
- [18] Y. Song, H. Kim, J.-H. Jang, W. Bai, C. Ye, J. Gu, Y. Bu, Pt3Ni alloy nanoparticle electro-catalysts with unique core-shell structure on oxygen-deficient layered perovskites for solid oxide cells, *Adv. Energy Mater.* 13 (2023) 230284, <https://doi.org/10.1002/aenm.202302384>.
- [19] Y. Zhu, J. Sunarso, W. Zhou and, Z. Shao, Probing CO<sub>2</sub> reaction mechanisms and effects on the  $\text{SrNb}_{0.1}\text{Co}_{0.9}\text{-}x\text{Fe}_{x}\text{O}_3\text{-}\delta$  cathodes for solid oxide fuel cells, *Appl. Catal. B* 172 (2015) 52–57, <https://doi.org/10.1016/j.apcatb.2015.02.010>.
- [20] C. Tang, K. Kousi, D. Neagu, J. Portoles, E.L. Papaioannou, I.S. Metcalfe, Towards efficient use of noble metals via exsolution exemplified for CO oxidation, *Nanoscale* 11 (2019) 16935–16944, <https://doi.org/10.1039/C9NR05617C>.
- [21] S. Joo, C. Lim, O. Kwon, L. Zhang, J. Zhou, J.-Q. Wang, H.Y. Jeong, Y.-W. Sin, S. Choi, G. Kim, The first observation of Ni nanoparticle exsolution from YSZ and its application for dry reforming of methane, *Mater. Rep.: Energy* 1 (2021) 100021, <https://doi.org/10.1016/j.matre.2021.100021>.
- [22] D. Skarmoutsos, P. Nikolopoulos, A. Tsoga, Titania doped YSZ for SOFC anode Ni-cermet, *Ionicics* 5 (1999) 455–459, <https://doi.org/10.1007/BF02376013>.
- [23] H.C.M. Knoops, T. Faraz, K. Arts, W.M.M. (Erwin) Kessels, Status and prospects of plasma-assisted atomic layer deposition, *J. Vac. Sci. Technol. A* 37 (2019) 030902, <https://doi.org/10.1116/1.5088582>.
- [24] J.M. Paige, D. Vu, T. Cao, S. McIntosh, R.J. Gorte, J.M. Vohs, Investigating the catalytic requirements of perovskite fuel electrodes using ultra-low metal loadings, *J. Electrochem. Soc.* 168 (2021) 084502, <https://doi.org/10.1149/1945-7111/ac1703>.
- [25] S. Kye, H.J. Kim, D. Go, B.C. Yang, J.W. Shin, S. Lee, J. An, Ultralow-loading ruthenium catalysts by plasma-enhanced atomic layer deposition for a solid oxide fuel cell, *ACS Catal.* 11 (2021) 3523–3529, <https://doi.org/10.1021/acscatal.0c04526>.
- [26] S.-S. Yim, D.-J. Lee, K.-S. Kim, K.-B. Kim, Atomic layer deposition of Ru nanocrystals with a tunable density and size for charge storage memory device

- application, *Electrochim. Solid-State Lett.* 11 (2008) K89, <https://doi.org/10.1149/1.2952432>.
- [27] Q. Fang, C. Hodson, C. Xu, R. Gunn, Nucleation and growth of platinum films on high-k/metal gate, *Phys. Procedia* 32 (2012) 55–560, <https://doi.org/10.1016/j.phpro.2012.03.600>.
- [28] C.D. Koolen, E. Oveisi, J. Zhang, M. Li, O.V. Safonova, J.K. Pedersen, J. Rossmeisl, W. Luo, A. Züttel, Low-temperature non-equilibrium synthesis of anisotropic multimetallic nanosurface alloys for electrochemical CO<sub>2</sub> reduction, *Nat. Synth.* 3 (2024) 47–57, <https://doi.org/10.1038/s44160-023-00387-3>.
- [29] Y. Liu, Z. Zheng, S. Jabeen, N. Liu, Y. Liu, Y. Cheng, Y. Li, J. Yu, X. Wu, N. Yan, L. Xu, H. Li, Mechanocatalytic route to fabricate an efficient nitrate reduction electrocatalyst, *Nano Res.* 17 (2024) 4889–4897, <https://doi.org/10.1007/s12274-024-6478-8>.
- [30] C.D. Koolen, W. Luo and, A. Züttel, From single crystal to single atom catalysts: structural factors influencing the performance of metal catalysts for CO<sub>2</sub> electroreduction, *ACS Catal.* 13 (2023) 948–973. (<https://pubs.acs.org/doi/10.1021/acscatal.2c03842>).
- [31] H.C.M. Knoops, A.J.M. Mackus, M.E. Donders, M.C.M. van de Sanden, P.H. L. Notten, W.M.M. Kessels, Remote plasma ALD of platinum and platinum oxide films, *Electrochim. Solid-State Lett.* 12 (2009) G34–G36, <https://doi.org/10.1149/1.3125876>.
- [32] F. Shen, R. Wang, M.C. Tucker, Long term durability test and post mortem for metal-supported solid oxide electrolysis cells, *J. Power Sources* 474 (2020) 228618, <https://doi.org/10.1016/j.jpowsour.2020.228618>.
- [33] P. Hohenberg, W. Kohn, Inhomogeneous electron gas, *Phys. Rev.* 136 (1964) B864, <https://doi.org/10.1103/PhysRev.136.B864>.
- [34] J.P. Perdew, K. Burke, M. Ernzerhof, Generalized gradient approximation made simple, *Phys. Rev. Lett.* 77 (1996) 3865, <https://doi.org/10.1103/PhysRevLett.77.3865>.
- [35] G. Kresse, D. Joubert, From ultrasoft pseudopotentials to the projector augmented-wave method, *Phys. Rev. B* 59 (1999) 1758, <https://doi.org/10.1103/PhysRevB.59.1758>.
- [36] G. Kresse, J. Furthmüller, Efficient iterative schemes for ab initio total-energy calculations using a plane-wave basis set, *Phys. Rev. B* 54 (1996) 11169, <https://doi.org/10.1103/PhysRevB.54.11169>.
- [37] A. Eguizabal, L. Uson, V. Sebastian, J.L. Hueso, M.P. Pina, Efficient and facile tuning of Vulcan XC72 with ultra-samll Pt particles for electrocatalytic applications, *RSC Adv.* 5 (2015) 90691–90697, <https://doi.org/10.1039/C5RA16698E>.
- [38] H.-S. Noh, J.-W. Son, H. Lee, H.-I. Ji, J.-H. Lee, H.-W. Lee, Suppression of Ni agglomeration in PLD fabricated Ni-YSZ composite for surface modification of SOFC anode, *J. Eur. Ceram. Soc.* 30 (2010) 3415–3423, <https://doi.org/10.1016/j.jeurceramsoc.2010.07.035>.
- [39] W. Zhou, Z.L. Wang, *Scanning microscopy for nanotechnology: techniques and applications*, 1st ed., Springer, New York, 2007.
- [40] Y. Chen, L. Liang, S.A.P. Navia, A. Hinerman, K. Gerdes, X. Song, Synergetic interaction of additive dual nanocatalysts to accelerate oxygen reduction reaction in fuel cell cathodes, *ACS Catal.* 9 (2019) 6664–6671, <https://doi.org/10.1021/acscatal.9b00811>.
- [41] N.W. Kwak, S.J. Jeong, H.G. Seo, S. Lee, Y. Kim, J.K. Kim, P. Byeon, S.-Y. Chung, W. Jung, In situ synthesis of supported metal nanocatalysts through heterogeneous doping, *Nat. Commun.* 9 (2018) 4829, <https://doi.org/10.1038/s41467-018-07050-y>.
- [42] D. McLean, A. Maradudin, Grain boundaries in metals, *Phys. Today* 11 (1958) 35–36, <https://doi.org/10.1063/1.3062568>.
- [43] P. Wynblatt, R.C. Ku, Surface energy and solute strain energy effects in surface segregation, *Surf. Sci.* 65 (1977) 511–531, [https://doi.org/10.1016/0039-6028\(77\)90462-9](https://doi.org/10.1016/0039-6028(77)90462-9).
- [44] S. Mukherjee, J.L. Morán-López, Surface segregation in transition-metal alloys and in bimetallic alloy clusters, *Surf. Sci.* 189 (1987) 1135–1142, [https://doi.org/10.1016/S0039-6028\(87\)80561-7](https://doi.org/10.1016/S0039-6028(87)80561-7).
- [45] S.B. Desu, D.A. Payne, Interfacial segregation in perovskites: II, Experimental evidence, *J. Am. Ceram. Soc.* 73 (1990) 3398–3406, <https://doi.org/10.1111/j.1151-2916.1990.tb06467.x>.
- [46] O.M. Løvvik, Surface segregation in palladium based alloys from density-functional calculations, *Surf. Sci.* 583 (2005) 100, <https://doi.org/10.1016/j.susc.2005.03.028>.
- [47] J.W. Han, J.R. Kitchin, D.S. Sholl, Step decoration of chiral metal surfaces, *J. Am. Ceram. Soc.* 130 (2009) 124710, <https://doi.org/10.1063/1.3096964>.
- [48] R. Tran, Z. Xu, N. Zhou, B. Radhakrishnan, J. Luo, S.P. Ong, Computational study of metallic dopant segregation and embrittlement at molybdenum grain boundaries, *Acta Mater.* 117 (2016) 91–99, <https://doi.org/10.1016/j.actamat.2016.07.005>.
- [49] B. Koo, K. Kim, J.K. Kim, H. Kwon, J.W. Han, W. Jung, Sr segregation in perovskite oxides: why it happens and how it exists, *Joule* 2 (2018) 1476–1499, <https://doi.org/10.1016/j.joule.2018.07.016>.
- [50] T. Takeguchi, R. kikuchi, T. Yano, K. Eguchi, K. Murata, Effect of precious metal addition to Ni-YSZ cermet on reforming of CH<sub>4</sub> and electrochemical activity as SOFC anode, *Catal. Today* 84 (2003) 217–222, [https://doi.org/10.1016/S0920-5861\(03\)00278-5](https://doi.org/10.1016/S0920-5861(03)00278-5).
- [51] T.-M. Ahn, J.K. Tien, P. Wynblatt, Coarsening kinetics of platinum particles on curved oxide substrates, *J. Catal.* 66 (1980) 335–346, [https://doi.org/10.1016/0021-9517\(80\)90038-X](https://doi.org/10.1016/0021-9517(80)90038-X).
- [52] M. Shishkin, T. Ziegler, The oxidation of H<sub>2</sub> and CH<sub>4</sub> on an oxygen-enriched yttria-stabilized zirconia surface: a theoretical study based on density functional theory, *J. Phys. Chem. C* 112 (2008) 19662–19669, <https://doi.org/10.1021/jp808049p>.
- [53] M. Shishkin, T. Ziegler, Hydrogen oxidation at the Ni/yttria-stabilized zirconia interface: a study based on density functional theory, *J. Phys. Chem. C* 114 (2010) 11209–11214, <https://doi.org/10.1021/jp1030575>.
- [54] M. Shishkin, T. Ziegler, Oxidation of H<sub>2</sub>, CH<sub>4</sub>, and CO molecules at the interface between nickel and yttria-stabilized zirconia: a theoretical study based on DFT, *J. Phys. Chem. C* 113 (2009) 21667–21678, <https://doi.org/10.1021/jp905615c>.
- [55] F. Che, S. Ha, J.-S. McEwen, Elucidating the role of the electric field at the Ni/YSZ electrode: a DFT study, *J. Phys. Chem. C* 120 (2016) 14608–14620, <https://doi.org/10.1021/acs.jpc.6b01292>.
- [56] J. Greeley, T.F. Jarillo, J. Bonde, L. Chorkendorff, J.K. Nørskov, Computational high-throughput screening of electrocatalytic materials for hydrogen evolution, *Nat. Mater.* 5 (2006) 909–913, <https://doi.org/10.1038/nmat1752>.